ISSN: 0067-2904

Seismotectonics and Seismic Source Parameters of the Mid-Eastern Iraq - Western Iran Using Moment Tensor Inversion Technique

Hasanain Jasim Mohammed[1], Ali M. Al-Rahim[2]*
[1]Department of Seismology, Iraqi Meteorological Organization and Seismology, Baghdad, Iraq
[2]University of Baghdad, College of Science, Department of Geology, Baghdad, Iraq

Received: 27/1/2020 Accepted: 23/3/2020

Abstract

The study area is encompassed by the 33.59-34.93°N latitudes and 45.44-46.39°E longitudes and divided into four groups with respect to earthquake event locations. We determined fault plane solutions, moment magnitudes, focal depths, and trend of slip with the direction of the moment stress axes (P, N, and T) for 102 earthquakes. These earthquakes had a local magnitude in the range between 4.0 and 6.4 for the time period from January 2018 to the end of August 2019, with focal depths ranged between 6 and 17 km. Waveform moment tensor inversion technique was used to analyze the database constructed from seismic stations on local and neighboring country networks (Iraq, Iran, and Turkey). We separated the studied events into four regional subsets (circles). The types of the obtained fault plane solutions are predominantly thrust fault and strike-slip, with the focal depths ranging from 8 to 21 km.

A new scaling relation between local magnitude (Ml) and the estimated moment magnitude (M*w*) has been developed utilizing a linear regression. Good match results obtained in the present research good match with both seismic trends concluded from earthquake locations and mapped faults. Generally, direction shows NW–SE striking focal planes corresponding with the tectonic framework of the Arabian–Eurasian continental collision zone. The anticlockwise rotation of the Arabian plate that appears accountable for strike-slip displacements on fault surfaces.

Keywords: Focal mechanism solutions, Moment tensor inversion, Moment stress axes, Seismotectonic, Iraq-Iran border.

الزلزالية التكتونية ومعاملات المصدر الزلزالي لمنطقة وسط شرق العراق–الجزء الغربي من إيران باستخدام تقنية انعكاس الشد العزمي

حسنين جاسم محمد[1] ، علي مكي حسين الرحيم*[2]
[1]قسم الرصد الزلزالي, الهيئة العامة للأنواء الجوية والرصد الزلزالي, بغداد, العراق
[2]جامعة بغداد, كلية العلوم, قسم علم الأرض, بغداد, العراق

الخلاصة

تقع منطقة الدراسة بين خطوط العرض 33.59–34.93° شمالا وخطوط الطول 45.44–46.39° شرقا وقسمت الى أربع مجاميع نسبة الى مواقع الاحداث الزلزالية. تم تحديد حلول ميكانيكية الصدوع , المقادير العزمية , الأعماق البؤرية واتجاه الانزلاق مع محاور الجهد العزمية (P , N و T) لـ 102 هزة أرضية .

*Email: alial_rahim@yahoo.com

هذه الهزات لها مقدار زلزالي محلي يتراوح بين 4.0 و6.4 خلال الفترة الزمنية من كانون الثاني 2018 الى نهاية آب 2019 مع أعماق بؤرية تراوحت بين 6 و17كم. استخدمت تقنية انعكاس الشد العزمي الموجي في تحليل قاعدة البيانات التي تم انشاؤها من شبكات محطات الرصد الزلزالي المحلية والمجاورة للبلد (العراق، إيران وتركيا). فصلنا الاحداث الزلزالية الى أربع مجاميع فرعية (دوائر). تم الحصول على أنواع حلول ميكانيكية البؤر الزلزالية ووجد ان الفوالق الاندفاعية هي السائدة مع عمق بؤري تراوح بين 8 الى 21كم. تم استنتاج علاقة جديدة بين المقدار المحلي (Ml) والمقدار العزمي المخمن (M_w) باستخدام طريقة الانحدار الخطي. تظهر النتائج التي تم الحصول عليها في هذا البحث توافقا جيدا مع الاتجاهات الزلزالية المستخلصة من مواقع الهزات الأرضية واتجاه الصدوع العامة. يبدو ان الحلول أعطت ميكانيكية صدوع بامتداد مستويات ذات اتجاه شمال غرب–جنوب شرق ومتوافق مع الإطار التكتوني لنطاق تصادم الصفيحة العربية مع الأوراسيوية. يظهر الدوران عكس عقارب الساعة للصفيحة العربية المسؤولية عن ازاحة انزلاقية – مضربية على أسطح الفوالق.

1. Introduction

Earthquakes are generally concentrated on the boundaries of tectonic plates [1].Important information about the tectonic features and structural styles of the subsurface geological structures could be considered from the analysis of earthquakes. Most of the Iraqi previous studies of the seismicity and seismotectonic parameters indicated that the levels of seismicity are moderate to high at northern and northeastern boundaries while decreasing towards the southern and southwestern [2, 3].
Focal mechanisms are the most effective tool in seismology to study the relative magnitudes and orientation of the stresses emitted during earthquakes. Seismologists refer to the direction of slip in an earthquake and the orientation of the fault on which it occurs as the focal mechanism. Different types of focal mechanisms can be described, which are displayed graphically by the so-called "beach ball" diagram. One of the fundamental techniques in studying active continental motions is seismic source analysis along with earthquake focal mechanism evaluation. These focal mechanisms could assist to determine the state and orientations of tectonic motions and to give a better understanding of the current mode of tectonic deformation in a certain region. The study area is located in the collision tectonics between the Arabian and the Iranian plate (Figure-1) between latitudes 33.59– 34.93°N and longitudes 45.44–46.39°E (Figure-2). These earthquakes have a moment magnitude of $4.0 \leq MW \leq 6.4$ that occurred in the region on the beginning January 2018 to the end of August 2019. Most events are located in the mid-eastern Iraq and western part of Iran, near to the borders. The reasons for most events occurring in the region are probably the stresses generated by the Arabian plate movement to the north and northeast and its collision with the Iranian-Turkish plateau, also in addition to the impact of neo tectonic activation of the upper crust [4]. Database from the region was subdivided into four groups; AA (Belula-Ezgeleh), BB (Khanaqin-Qasre Shirin-Sarpol Zahab), CC (Mandali-Samoor), and DD (Qolqoleh-Halol), according to the spatial distribution of the events (Figure-3). The aim of this study is to use moment tensor inversion technique to determine fault plane solutions, moment magnitudes, and focal depths according to a previously described approach [9].

2. Tectonic and Structure Setting

Iraq is located at the extreme northeastern part of the Arabian Plate, which is in collision with the Eurasian Plate and surrounded by regions of relatively high seismicity. This collision still continues forward and has caused alignment of the gradually developed structures in NW-SE trend mainly, particularly in the northern, northeastern and eastern sides of Iraq. However, many transversal linear elements of the NE-SW trend, represented through rivers, streams, valleys, playas, anticlines and offsets, are developed, in a parallel trend to the major compressional forces created by the aforementioned collision [10]. In recently active tectonic areas, the topography of the land surface is an accurate reflection of the underlying structure and its interaction with surface processes [11].

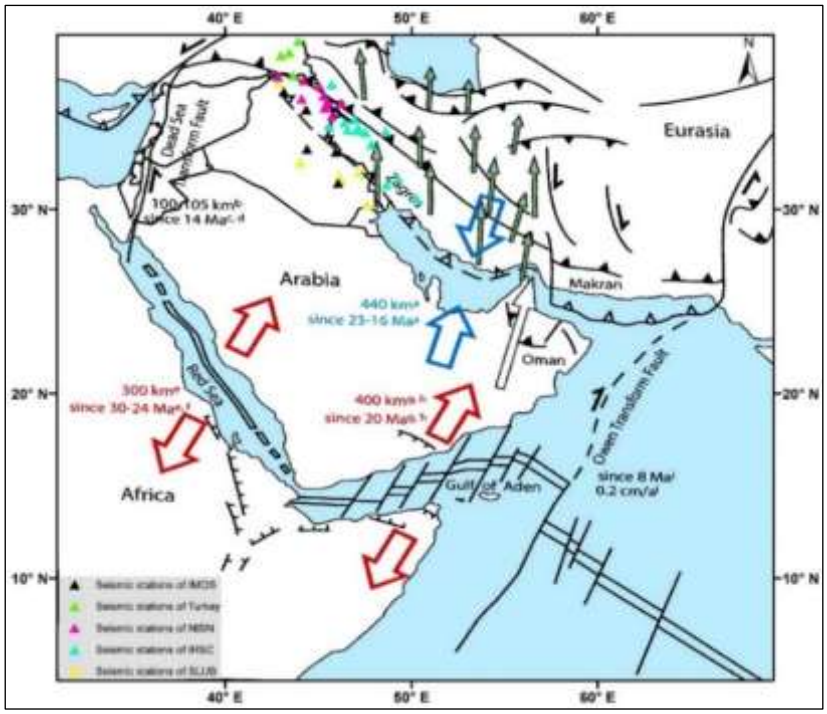

Figure 1- Location of Iraq within the Arabia-Eurasia collision zone and major tectonic setting of the Arabian Plate. Large red and blue colored symbols simplify divergence and convergence movements with overall amount and age, respectively. Smaller green arrows show present-day GPS values with respect to fixed Europa from Iran and white arrow from Oman [5]; triangles represent geographic distribution of seismic stations (Table-1) using waveform inversion in this study.

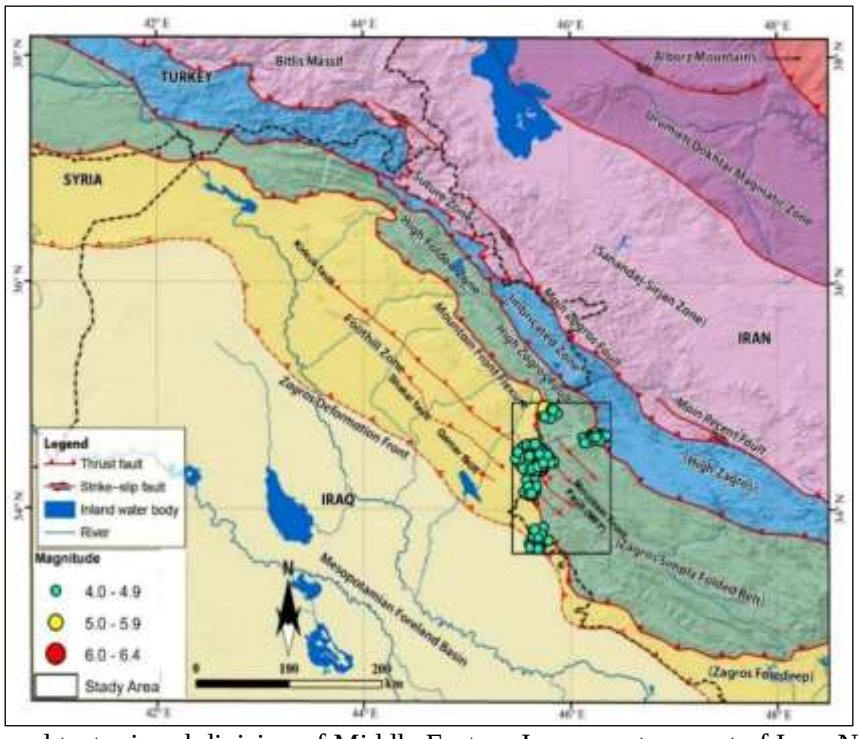

Figure 2- Regional tectonic subdivision of Middle Eastern Iraq - western part of Iran. Names within the parentheses are known in the Iranian part of Zagros (modified after [6]); [7, 8]. The black rectangle represents the study area plotted in Figure-3, and the magnitude of the 102 earthquakes is indicated by the diameter of the colored circles.

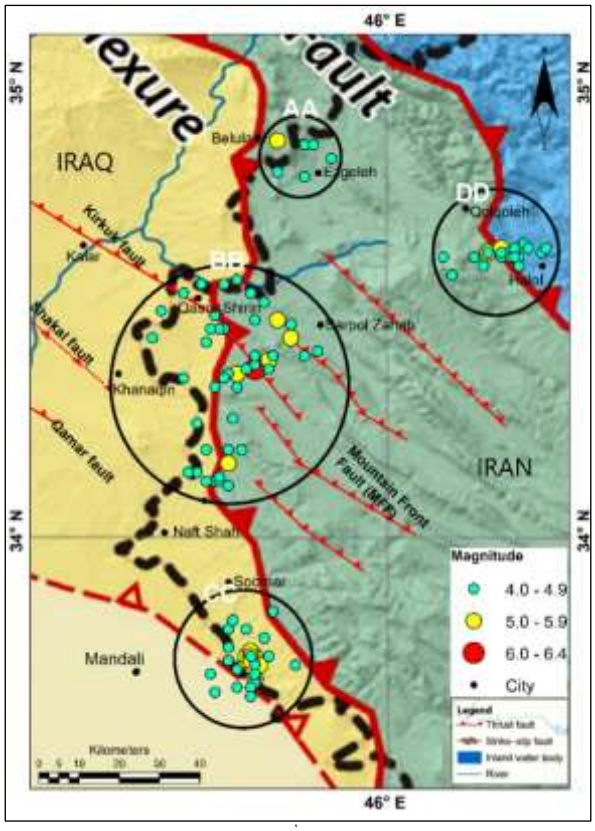

Figure 3- Simplified map of the locations and magnitudes distribution for 102 earthquakes (January 2018-August 2019) and the main tectonic boundaries. The earthquakes are clustered into four groups and indicated by black circles; AA (Belula-Ezgeleh), BB (Khanaqin-Qasre Shirin-Sarpol Zahab), CC (Mandali-Samoor), and DD (Qolqoleh-Halol), the data of which were collected from the Iraqi Meteorological Organization and Seismology (IMOS).

Generally, the Zagros Fold–Thrust Belt (including the study area) is one of the most seismically active belts in Asia. The SW-Vergence fold-thrust belt and circumferential foreland basin were formed as a result of the Arabia-Eurasia collision during final closure of the Neotethys Ocean [12].

The intensity of deformation, age of the sedimentary units and amount of shortening in the study region showed a reduction from north and northeast (Zagros Suture Zone) in the direction of SW (Foreland region) [13].The NW portion of the Zagros Fold–Thrust Belt is subdivided into zones depending on the topography and deformational style, with the zones from NE to SW are Zagros Suture Zone, Imbricated Zone, High Folded Zone, and Foothill Zone (Fig. 2 in [14]).

One of the morphologically generality distinguished, structural elements of the Zagros Fold–Thrust Belt is the Mountain Front Flexure (MFF), which separates the High Folded Zone and the Foothill Zone (these zones are known as a part of the Zagros Simply Folded Belt and Zagros Foredeep in Iran, respectively; Fig.2). These include the folding of sedimentary rocks which are expressed at the surface by a series of anticlines and synclines which dominate the range physiography [15]. The Foothill Zone is divided by the Kirkuk Fault into the Chemchamal and the Hemrin Subzone [14]. Major NW-SE trending and SW dipping back thrust faults are also one of the feature structures in this zone [14, 16, 17, 18, 19]. Tectonic research reported that the Iranian plateau features a high density of energetic and recent faults along with reverse faulting with large strike-slip component (i.e., dextral-reverse oblique slip near the impinging zone). Pure thrust faulting tends to dominate the tectonics of the region toward central Iran [20]. Territorial shortening along the major thrust systems, that are accountable for producing strong earthquakes in northeast Iran, is about 1–2 mm/year, using optically stimulated luminescence (OSL) dating of river deposits [21]. The GPS data denote that the average of north-south shortening from Arabia to Eurasia is nearly 2–2.5 cm/year [22]. Nevertheless, the continental convergence between Arabia and Eurasia is stationary at 2 to 3 cm/year since 56 Ma [23].

3. Data set preparation and processing

From January 2018 to August 2019, the IRSC catalogue has 102 earthquakes in the study area at depths of 06–17 km with $4.0 \leq Ml \leq 6.4$. The waveform data, gathered from five local seismic stations and contiguous networks including 39 stations, belong to the Iraqi Meteorological Organization and Seismology (IMOS), North Iraq Seismographic Network (NISN), Iraq Seismological Laboratory of University of Basrah (SLUB), Iranian Seismological Center (IRSC), and Kandilli Observatory and Earthquake Research Institute (KOERI)-Turkey (Fig.1 and Table-1). Most broadband stations usually record 100 samples per second. A perfect azimuthal coverage is taken into consideration around the source, being very desirable and critical to such focal mechanism solution studies. The epicentral distances between the stations and seismic events were less than 600 km. The origin parameters of the events were chosen from the seismic catalogue of the Iranian Seismological Center (IRSC) and listed in Table- 2. The original seismic data format is in MiniSEED or SEISAN format (i.e., IMOS, IRSC and NISN) and needed to be transformed into SAC and then GSAC formats. The header file for all data files required preparation before the execution of the analysis software. An instrument response correction was applied for each seismic event during the processing steps, using deconvolution response file for each seismometer. Three components (Vertical Z, North-South N, and East-West E directions) were presented for each recorded event. These three components needed to be rotated from a station-based recording system (ZNE) to an event-based recording system (ZRT). The ZRT rotation system is a 2D rotation where the Z component is still pointing in the same direction as in the original ZNE recording, while the two horizontal components N and E are rotated into the radial R and tangential T components, respectively.

Table 1- Locations and names of seismic stations that are used in the current study

Network name	Station code	Latitude	Longitude	Elev. (m)	Network name	Station code	Latitude	Longitude	Elev. (m)
Iraqi Meteorological Organization and Seismology (IMOS)	BHD	33.274	44.386	32	Iranian Seismological Center (IRSC	DHR	34.700	46.386	1434
	IBDR	33.113	45.934	70		GHG	34.329	46.569	2090
	IKRK	35.400	44.340	331		KOM	34.176	47.514	1502
	MSL	36.382	43.148	242		LIN	34.919	46.962	2195
	RAFI	31.430	46.060	9		HSAM	34.212	48.602	2314
North Iraq Seismographic Network (NISN)	KSBB	35.042	45.709	550		ABH1	30.600	50.253	346
	KSSS	35.770	46.236	1515		AHWZ	31.330	48.644	19
	KSWW	36.149	45.262	1310		AMIS	31.665	49.287	442
	KSJS	35.497	45.345	825		KCHF	34.275	47.040	1715
	KEHH	36.676	45.047	1725		KER	34.387	47.133	1338
	KESM	36.985	44.198	1000		KGS1	34.506	45.589	362
	KDDA	37.213	42.821	750		KFM	33.524	47.847	1676
	KEKZ	35.989	44.097	450		MAHB	36.767	45.705	1370
	SLY	35.632	45.469	1485	Iraq Seismological Laboratory of University of Basrah (SLUB)	AMR2	31.990	47.190	7
	KI01	35.848	45.495	1335		BSR2	30.293	47.619	17
Turkey-Kandilli Observatory and Earthquake Research Institute (KOERI)	CUKT	37.247	43.608	1300		DHK1	36.861	42.867	766
	AKDM	38.329	42.980	1662		KAR2	32.540	44.024	43
	CLDR	39.144	43.917	2094		NSR1	31.742	46.115	14
	VANB	38.509	43.406	1227		NSR4	31.540	46.202	8

4. Methodology

The Computer Programs in Seismology (CPS) version 3.30 was used in the present work as previously described [9]. LINUX platform was also applied, which includes 149 programs that can be run using scripts. In general, the requirements of performing the data and source inversion routines in seismology are waveform data, instrument response, station locations, earthquake location, velocity model, Green's functions and results assessment.

Table 2- Source parameters from (Iranian seismological center catalog) and focal mechanism solutions of the 112 earthquakes from the moment tensor inversion

Date	O. Time (UTC)	Lat .N	Long .E	RD	Ml	CD	M_W	Mo dyne-cm	Plane 1			Plane 2			Moment Stress Axes					
															P		N		T	
									S	D	R	S	D	R	PL	AZ	PL	AZ	PL	AZ
2018/01/05	6:32:57	34.530	45.698	8	4	19	4	1.26e+22	181	78	99	325	15	55	32	264	9	359	56	102
2018/01/06	15:22:08	34.471	45.759	10	5	17	5.02	4.27e+23	360	80	75	237	18	146	33	103	15	3	53	252
2018/01/11	6:59:29	33.712	45.693	8	5.6	20	5.63	3.51e+24	135	65	70	356	32	126	18	240	18	144	64	11
2018/01/11	7:00:53	33.667	45.714	12	5.1	16	5.28	1.05e+24	166	54	110	315	40	65	07	243	16	335	72	128
2018/01/11	7:14:15	33.722	45.709	9	5.4	18	5.28	1.05e+24	160	65	90	340	25	90	20	250	00	340	70	70
2018/01/11	7:21:33	33.700	45.719	12	5.2	19	5.27	1.01e+24	315	75	75	181	21	134	28	57	14	319	57	205
2018/01/11	7:37:09	33.762	45.731	12	4.2	21	4.02	1.35e+22	310	60	60	179	41	131	10	61	26	326	62	171
2018/01/11	7:52:47	33.815	45.747	12	4.3	17	4.11	1.84e+22	177	57	130	300	50	45	4	240	33	333	57	144
2018/01/11	7:55:00	33.733	45.703	8	5.1	18	4.8	2.00e+23	150	80	70	34	22	153	32	257	20	154	51	37
2018/01/11	8:00:39	33.724	45.686	11	5.4	18	5.28	1.05e+24	167	67	99	325	25	70	21	250	08	343	67	94
2018/01/11	8:17:55	33.641	45.622	8	4.1	17	3.98	1.17e+22	150	50	90	330	40	90	5	240	0	150	85	60
2018/01/11	8:29:03	33.804	45.659	12	4	18	3.82	6.76e+21	330	80	50	228	41	165	24	90	39	338	41	165
2018/01/11	9:23:55	33.677	45.706	13	4.1	19	3.9	8.91e+21	130	65	65	358	35	132	16	238	23	141	62	1
2018/01/11	9:32:24	33.706	45.653	8	4.2	18	4.12	1.91e+22	155	55	100	318	36	76	9	238	8	329	77	99
2018/01/11	13:16:43	33.724	45.735	8	4.3	18	4.21	2.60e+22	145	65	80	348	27	110	19	242	9	149	68	35
2018/01/11	13:30:46	33.740	45.654	8	4.1	17	3.91	9.23e+22	165	60	109	310	35	60	13	241	17	335	69	115
2018/01/11	14:47:17	33.723	45.699	9	4	20	4.01	1.30e+22	330	80	55	226	36	163	27	87	34	337	44	206
2018/01/11	20:19:40	33.653	45.697	8	4	18	3.81	6.53e+21	168	62	101	325	30	70	16	250	10	342	71	102
2018/01/11	21:50:44	33.775	45.685	8	4.4	19	4.31	3.67e+22	140	70	30	39	62	157	5	268	54	171	35	2
2018/01/11	21:52:22	33.779	45.648	8	4.3	20	3.77	5.69e+21	330	80	80	195	14	135	34	69	10	332	54	228
2018/01/12	17:50:40	33.645	45.671	7	4.3	16	3.88	8.32e+21	285	65	35	179	59	150	4	50	48	316	42	144
2018/01/13	0:33:26	33.660	45.708	8	4.2	19	4.27	3.20e+22	140	50	60	2	48	121	1	251	23	160	67	343
2018/01/13	6:30:30	33.671	45.707	8	4.3	17	3.81	6.53e+21	332	66	123	95	40	40	14	39	29	137	56	286
2018/01/13	9:24:19	33.718	45.699	12	4.2	19	4.21	2.60e+22	140	50	65	356	46	117	2	247	19	157	71	343
2018/01/14	19:45:47	34.396	45.851	8	4	17	4.11	1.84e+22	260	85	15	169	75	175	7	33	74	278	14	125
2018/01/18	16:48:42	34.556	45.669	9	4	15	3.92	9.55e+22	192	82	114	300	25	20	33	262	23	8	48	127
2018/01/19	22:17:56	33.709	45.699	9	5	16	4.91	2.92e+23	333	61	118	105	40	50	11	43	24	138	63	290
2018/01/21	2:19:37	34.528	45.547	17	4.1	14	4.03	1.48e+22	2	76	104	135	20	45	30	80	14	178	57	290
2018/01/21	5:45:39	34.548	45.586	16	4.1	16	4.05	1.50e+22	177	74	102	320	20	55	28	257	11	353	60	103
2018/01/26	20:17:34	33.675	45.611	8	4.4	13	4.09	1.72e+22	163	54	127	290	50	50	2	227	29	318	60	133
2018/02/02	9:42:57	34.798	45.757	8	4	8	4.16	2.19e+22	145	80	45	45	46	166	22	358	44	245	38	106
2018/02/16	18:22:00	33.634	45.699	12	4	18	3.97	1.14e+22	155	89	95	255	5	10	44	240	5	335	46	70
2018/03/28	0:27:05	34.491	45.497	17	4	19	3.95	1.06e+22	161	78	99	305	15	55	32	244	9	339	56	82
2018/04/01	8:35:25	34.434	45.786	7	5.3	15	5.13	6.24e+23	08	69	-148	265	60	-25	38	229	52	38	05	135
2018/04/02	3:03:22	34.388	45.821	7	4	14	4.01	1.30e+22	7	73	132	115	45	25	17	157	40	262	45	49
2018/04/30	22:14:49	34.861	45.821	8	4	18	4.15	2.11e+22	140	55	60	5	45	126	6	296	24	203	65	38
2018/05/22	0:31:53	34.830	45.879	12	4.4	16	4.35	4.22e+22	94	85	170	185	80	5	4	140	79	248	11	49
2018/06/26	17:57:03	34.618	46.268	8	4.8	15	4.54	8.13e+22	255	85	15	164	75	175	7	298	74	183	14	30
2018/06/26	22:13:05	34.546	45.641	14	4.1	14	3.77	5.69e+21	146	71	95	310	20	75	26	232	5	324	64	65
2018/07/15	7:10:59	34.614	46.278	8	4.6	17	4.32	3.80e+22	245	90	20	155	70	180	14	288	70	155	14	22
2018/07/16	5:33:53	34.625	46.289	8	4.2	14	4.16	2.19e+22	133	81	-160	40	70	-10	21	268	68	67	7	175
2018/07/22	10:07:25	34.630	46.255	8	5.7	15	5.52	2.40e+24	343	80	-165	250	75	-10	18	117	72	284	4	26
2018/07/22	16:48:47	34.585	46.296	6	4	13	3.98	1.17e+22	337	86	-150	245	60	-5	24	115	60	255	17	17
2018/07/23	0:59:47	34.606	46.303	6	4.4	16	4.37	4.52e+22	156	85	-170	65	80	-5	11	21	79	182	4	290
2018/07/24	8:46:11	34.643	46.312	8	4.5	16	4.29	3.43e+22	158	80	170	250	80	10	0	114	76	205	14	24
2018/07/24	19:58:29	34.794	45.816	6	4.4	14	4.5	7.08e+22	355	50	75	197	42	107	4	6	11	275	78	114
2018/07/25	1:47:47	34.634	46.315	9	4.2	17	4.02	1.35e+22	147	80	165	240	75	10	4	104	72	206	18	13
2018/07/26	15:51:19	34.317	45.622	12	4	17	4.15	2.11e+22	331	76	96	125	15	65	31	55	6	149	58	249
2018/08/04	17:02:04	34.620	46.354	8	4.1	12	3.75	5.31e+21	344	76	-164	250	75	-15	21	117	69	296	0	27
2018/08/25	22:13:25	34.622	46.233	8	5.9	13	5.82	6.76e+24	250	75	-30	348	61	-162	45	185	38	43	20	296
2018/08/26	5:18:28	34.622	46.231	9	4	16	4.05	1.50e+22	147	83	-135	50	45	-10	36	289	44	64	24	180
2018/08/26	8:25:03	34.620	46.259	8	4	11	3.67	4.01e+21	153	77	-149	55	60	-15	31	288	57	83	11	191
2018/08/26	9:23:33	34.608	46.202	7	4.1	12	3.67	4.03e+21	159	76	154	255	65	15	8	299	61	43	28	205
2018/08/29	5:34:35	34.613	46.291	8	4.6	11	4.12	1.91e+22	164	76	-164	70	75	-15	21	27	69	206	0	297
2018/08/31	21:05:43	34.608	46.127	8	4.9	13	4.73	1.57e+23	245	70	-25	344	67	-158	32	204	58	29	2	295
2018/09/01	5:31:10	34.344	45.545	12	4.5	16	4.17	2.26e+22	145	75	70	20	25	142	27	251	19	150	56	30
2018/09/09	23:53:54	34.455	45.794	6	4	16	3.78	5.89e+21	335	80	100	110	14	45	34	56	10	153	54	257
2018/09/13	17:05:10	34.612	46.195	9	4.1	14	3.8	6.31e+21	265	85	30	172	60	174	17	125	60	4	24	223
2018/09/19	19:29:19	33.693	45.673	8	4.3	17	4.13	1.97e+22	335	80	75	212	18	146	33	78	15	338	53	227
2018/09/30	23:49:24	34.609	46.255	8	4.4	16	4.13	1.97e+22	250	90	25	160	65	180	17	292	65	160	17	28
2018/10/17	03:16:54	34.433	45.475	10	4.5	18	4.76	1.74e+23	177	56	113	320	40	60	09	251	19	344	69	138
2018/11/05	20:32:07	34.618	46.285	8	4.4	16	4.14	2.04e+22	165	76	159	260	70	15	04	213	65	312	24	121
2018/11/17	19:19:03	34.609	46.293	6	4.1	13	4.15	2.11e+22	250	75	-30	348	61	-163	32	206	57	46	09	302
2018/11/19	22:37:41	34.566	46.145	8	4	17	4.05	1.50e+22	248	81	-160	255	70	-10	21	213	68	12	07	120
2018/11/25	16:37:31	34.359	45.712	11	6.4	20	6.11	2.88e+25	135	80	-15	228	75	-170	18	91	72	282	03	182
2018/11/25	16:41:11	34.372	45.707	9	4.4	15	4.75	1.68e+23	355	80	35	258	56	168	16	122	54	09	31	222
2018/11/25	17:09:36	34.348	45.665	7	5.2	15	4.97	3.59e+23	175	84	98	305	10	40	38	259	8	355	51	94
2018/11/25	17:21:05	34.342	45.636	9	4	18	4.05	1.05e+22	316	71	95	120	20	75	26	42	5	134	64	235
2018/11/25	17:26:59	34.359	45.688	11	4	16	3.99	1.22e+22	150	80	75	27	18	146	33	253	15	153	53	42
2018/11/25	17:31:19	34.388	45.747	8	4	19	3.98	1.17e+22	348	71	107	125	25	50	24	56	16	162	60	282
2018/11/25	20:42:41	34.184	45.650	9	4.3	16	3.93	9.89e+21	150	60	85	340	30	99	15	244	04	152	74	47
2018/11/25	20:56:38	34.177	45.602	8	4.1	14	4.13	1.97e+22	165	73	88	351	17	96	21	162	69	341	0	72
2018/11/25	23:00:46	34.246	45.659	9	4.7	15	4.20	2.51e+22	184	66	108	325	30	55	19	260	17	356	64	125

2018/11/26	0:38:36	34.379	45.742	8	5.3	19	5.04	4.57e+23	356	85	-165	265	75	-05	14	222	74	14	07	130
2018/11/26	1:19:42	34.349	45.654	9	4.6	20	4.43	5.56e+22	336	76	95	135	15	70	31	61	05	154	59	253
2018/11/27	6:36:34	34.385	45.707	8	4.3	19	4.19	2.43e+22	162	68	125	280	40	35	16	227	32	328	53	114
2018/11/27	23:50:10	34.320	45.666	11	4.1	20	4.15	2.11e+22	140	75	75	06	21	134	28	242	14	144	57	30
2018/11/29	13:16:23	34.175	45.682	12	4.2	18	3.90	8.91e+21	164	73	115	285	30	35	24	234	24	336	55	105
2018/12/09	3:24:11	34.364	45.744	10	4.5	13	4.32	3.80e+22	340	70	75	198	25	125	24	82	14	345	62	227
2018/12/27	22:57:02	34.468	45.712	11	4	15	3.79	6.10e+21	155	80	90	335	10	90	35	245	0	155	55	65
2019/01/06	13:41:59	34.151	45.648	11	5.8	16	5.71	4.62e+24	337	56	100	135	35	75	11	146	09	237	76	5
2019/01/06	13:46:48	34.126	45.559	8	4.2	16	4.4	5.01e+22	169	77	128	275	40	20	23	231	37	340	44	117
2019/01/06	13:55:06	34.134	45.576	8	4.3	16	4.15	2.11e+22	4	58	138	120	55	40	02	153	39	244	51	60
2019/01/06	14:15:08	34.098	45.649	12	4.7	19	4.62	1.07e+23	140	70	75	358	25	125	24	242	14	145	62	27
2019/01/06	14:29:24	34.114	45.597	8	4.1	19	3.92	9.55e+21	155	80	70	39	22	153	32	262	20	159	51	42
2019/01/14	18:17:59	34.112	45.618	11	4.5	15	4.4	9.23e+21	336	72	88	344	18	96	05	27	58	124	31	294
2019/01/15	0:56:21	34.107	45.629	11	4	14	3.76	5.50e+21	135	75	30	36	61	163	09	263	57	159	32	337
2019/01/15	17:07:01	34.123	45.626	9	4	14	3.71	4.62e+21	188	71	137	295	50	25	13	246	44	349	43	144
2019/03/12	12:06:06	34.243	45.580	8	4.5	15	4.51	7.33e+22	155	59	106	305	35	65	12	323	14	56	71	193
2019/04/01	10:07:24	33.717	45.697	16	5.1	19	4.83	2.21e+23	347	68	125	105	40	35	16	52	32	153	53	299
2019/04/01	10:16:14	33.704	45.713	16	4.7	19	4.63	1.11e+23	324	60	87	150	30	95	15	56	02	326	75	226
2019/04/01	10:53:36	33.702	45.799	17	4.3	17	4.2	2.51e+22	340	60	125	105	45	45	08	45	30	140	59	301
2019/04/15	6:34:31	34.507	45.731	11	4.3	17	4.08	1.66e+22	340	80	80	205	14	135	34	79	10	342	54	238
2019/05/11	10:28:58	34.870	45.755	8	5.1	13	4.92	3.02e+23	12	73	132	120	45	25	17	72	40	177	45	324
2019/05/25	10:20:44	34.634	46.359	8	4.1	19	4.35	4.22e+22	305	75	-50	52	42	-157	45	255	38	113	20	06
2019/05/25	18:26:42	34.863	45.837	7	4	18	4.01	1.30e+22	40	78	144	140	55	15	15	05	52	115	34	265
2019/06/05	3:33:05	34.419	45.603	12	4.5	18	4.54	8.13e+22	160	70	90	340	20	90	25	250	0	340	65	70
2019/06/05	3:36:16	34.447	45.636	9	4.8	14	4.61	1.04e+23	172	57	130	295	50	45	04	145	33	238	57	49
2019/06/23	16:51:59	34.451	45.626	12	4.3	18	4.43	5.56e+22	176	62	112	315	35	55	14	250	19	345	66	125
2019/07/17	15:19:33	34.452	45.614	13	4.2	16	4.18	2.34e+22	290	60	45	173	52	141	05	50	38	317	52	146
2019/07/29	20:47:10	34.483	45.617	14	4.4	14	4.2	2.51e+22	335	50	90	155	40	90	05	65	0	155	85	245
2019/08/03	00:26:06	34.590	46.223	8	4.1	17	4.02	1.35e+22	330	79	139	70	50	15	18	296	48	47	36	142

O. Time (UTC) original time in UTC, Lat latitude in degree, Log longitude in degree, RD reported depth, Ml reported magnitude, CD calculated depth measured in kilometer (km), M_W moment magnitude, Mo seismic moment measured in dyne-cm, S strike, D depth measured in km, R rake angle, P, N, and T compressional, normal, and tensional moment stress axes, respectively, PL plunge angle, AZ azimuth.

4.1 Green's functions (GF) is created and described based on model assumptions or empirically gained data and includes wave propagation from the seismic source to a receiver, in response to specific source excitation. In the framework of source inversion problems, they are used to build synthetic seismograms, which are compared to real surface data records in the moment tensor inversion [24]. The use of the suitable regional velocity model is significant not only to correspond to the waveforms but also to define the moment magnitude of the earthquake, because the theoretical amplitudes at high frequencies depend very highly on the velocity model. Synthetic waveforms were calculated using a 1D-velocity model (Table 3) which is modified from the global IASPEI91 model in crustal part. This synthetic waveform was used later for calculating Green's functions needed for moment tensor inversion [25] Figure-4.

Table 3- Velocity and density values with layer thickness for the iraq2, which are used to build Green's functions of the study region, modified from the global IASPEI91 model [25]

Iraq2			
Thickness (km)	VP (km/s)	VS (km/s)	Density (gm/cm3)
1.00	2.80	1.62	2.05
5.00	5.23	3.02	2.50
9.00	6.18	3.57	2.70
10.00	6.20	3.58	2.70
11.00	6.50	3.75	2.70
50.00	7.88	4.55	3.14

4.2 Moment Tensor Inversion of Seismic Waveforms

Moment tensor is a mathematical characterization of seismic source that depends on wave propagation, earth model and synthetic seismograms. Moment tensor solution method is used to give a better assessment of seismic moment energy released from earthquakes and to identify the stress regime system and faults orientation for different seismic sources in the region. Moment magnitude

(Mw), Seismic Moment (Mo) and data for seismic source process are acquired by this procedure. Least square fitting of amplitude and/or waveform data can be derived from seismograms moment tensor components [26]. The waveform inversion method was used, which is based on the grid search method that involves the inspection of over all possible focal mechanism solutions. In general, the steps of performing moment tensor inversion are shown in the flowchart (Figure-5). The steps are explained in detail in appendix B of a previous study [27]. The moment tensor solutions have a quality factor assigned by the number of stations used during the inversion and the goodness of fit between synthetic and observed data. The inversion technique was applied as in the example in Figure-(6a). Seismic stations were used for the moment tensor inversion method solution of the event 2018/01/11 08:00:39 UTC. A grid search over the strike, dip and rake angles were used for every depth from 0.5 to 39 km in increments of one km, as shown in Figure-(6c). Figure-(6b) indicates the correlation and percentages between the observed (red traces) and predicted (blue traces) values.

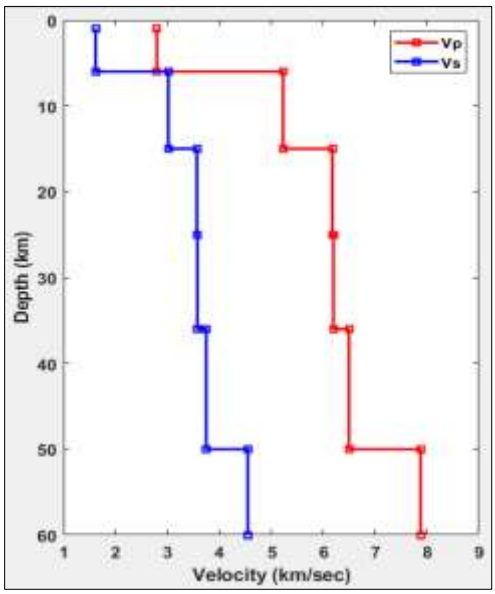

Figure 4- Velocity (Iraq2) versus depth plots for the model used to build Green's functions of the study region, modified from the global IASPEI91 model [25].

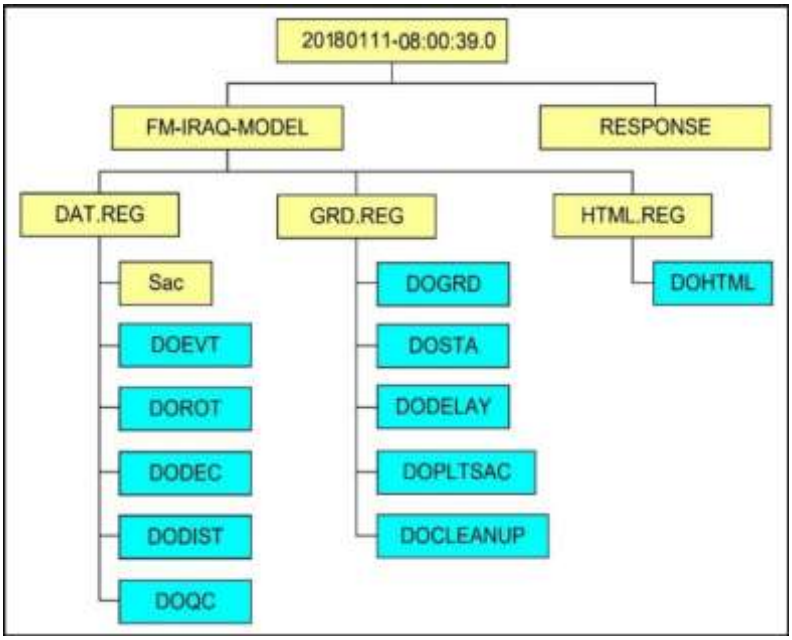

Figure 5- A flow chart of the Main directory and subdirectories used to perform the moment tensor inversion method (yellow boxes) and scripts (Turquoise boxes) [modified after 27].

The three components of the seismic record are R (Radial), Z (Vertical), and T (Transverse). Waveforms were plotted using the same scale. Peak amplitudes were indicated by the numbers to the left of each trace and contain pair of numbers that indicate the time shift required for maximum correlation between the observed and predicted traces. Percentage of variance reduction was used to characterize the individual goodness of fitness (100% indicates a perfect fit). To improve the signal-to-noise ratios (SNRs), the waveforms were filtered in frequency bands that were individually adjusted according to the data characteristics and quality. All traces in Figure-(6b) represent ground velocity (m/s) filtered in the 0.05-0.15 Hz band. Some traces were also removed because of noise, which may be due to site effects and instrumentation (i.e., in KGS1, AMR2 and KAR2 stations, only the vertical component remained, while traces R and T components in Figure- (6b) were rejected.

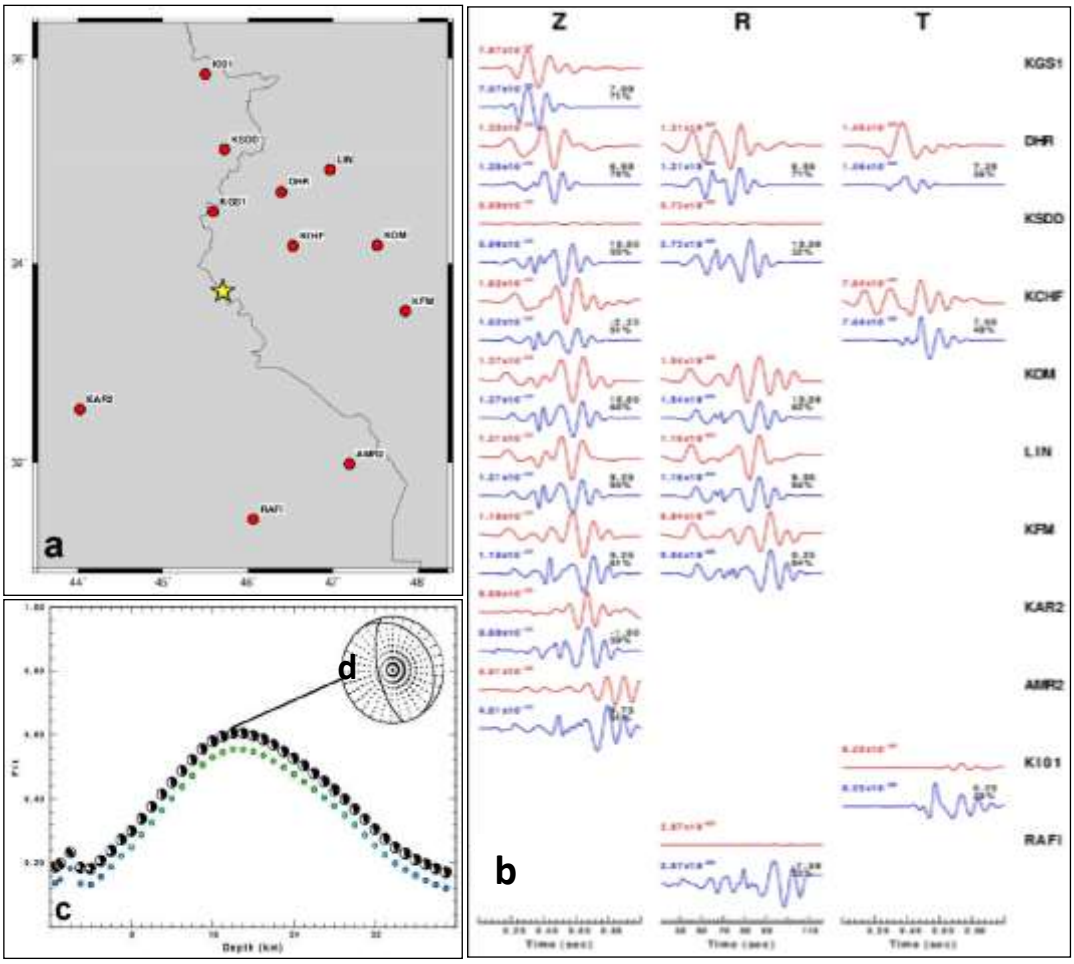

Figure 6- (a) Location of seismic stations (red colors) used for waveform inversion in moment tensor solution method. The star represents the location of the event 2018/01/11 08:00:39 UTC. (b) Correlation and percentages between observed (red) and predicted (blue) traces. The three components of the seismic record are R (Radial), Z (Vertical), and T (Transverse). Each observed-predicted component is plotted using the same scale and the numbers to the left of each trace indicate peak amplitudes. A pair of numbers is given in black at the right side of each predicted traces indicate: (i) the upper number, the time shift required for maximum correlation between the observed and predicted traces and (ii) percentage of variance reduction to characterize the individual goodness of fit. (c) The best fit as a function of depth sensitivity. The best fit value is 0.5560 and indicates a depth of 18 km. (d) Waveform inversion focal mechanism, the beach-ball shows the best solution at this depth.

5. Results

5.1 Classification of Focal Mechanism Solutions

Detailed information on the resulting focal mechanisms are listed in (Table-2) and include the strike orientation, dip angle, rake angle of both nodal planes, the direction of slip, and the orientations

of the moment stress axes. These are calculated by a moment tensor inversion technique for 102 events. The beach balls were plotted for each group using color coding according to the focal mechanism type: red for normal with strike slip faulting, green for strike slip, blue for thrust pure or with strike slip faulting, and gray for unknown or oblique type that indicates the maximum horizontal stress azimuth that is not defined. Figure-7 shows the beach balls for the group AA (Belula-Ezgeleh) plots for northeastern Iraq which have a dominance of thrust with strike slip (TS) and a few strike-slip (SS) focal mechanisms, while the plots for the groups BB (Khanaqin-Qasre Shirin-Sarpol Zahab) and CC (Mandali-Samoor) show a predominance of thrust (TF), thrust with strike slip (TS) and some strike-slip (SS) focal mechanisms. Finally, all focal mechanisms with a group DD (Qolqoleh-Halol) have a relatively strike-slip (SS), except for one event with a normal with strike slip (NS). In general, the largest number of earthquakes with the highest energy happens in the upper 40 Kilometers of the earth's crust [28]. Regarding the focal mechanism depths solution of earthquakes in the study region, it ranged from 8 to 21 km, while the reported focal depths ranged between 6 and 17 km (Table 2).

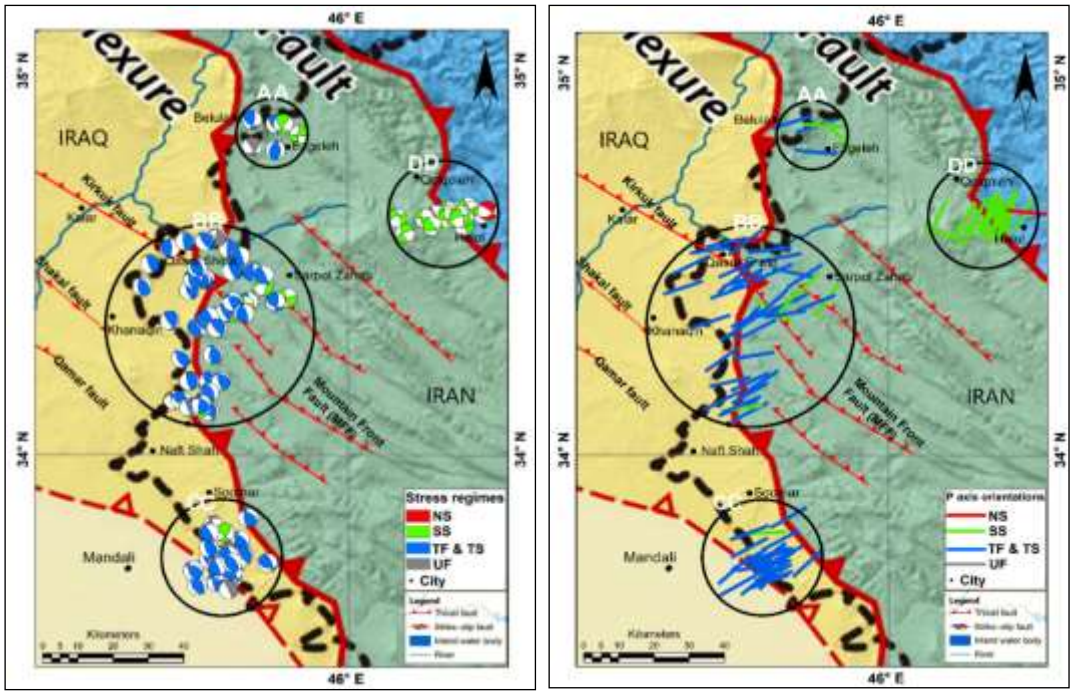

Figure 7- (Left) Focal mechanism colored for 102 events is proportional to moment tensor inversion and subdivided into four groups AA (Belula-Ezgeleh), BB(Khanaqin-Qasre Shirin-Sarpol Zahab), CC (Mandali-Samoor), and DD (Qolqoleh-Halol) according to the spatial distribution of the events. (Right) Compressional (P) moment stress axes from moment tensor solutions data based on (Table 2). The lines colors indicate the type of faulting: red, normal with strike slip (NS); blue, thrust or thrust with strike-slip (TF or TS respectively); and green, strike-slip.

5.2 Moment stress axes

The moment stress axes (P, N, and T for, respectively, maximum shortening, neutral axes and maximum extension) are perpendicular to each other from both the fault and the auxiliary planes. The same is correct for σ1, σ2 and σ3, only in the state of new fracture generation in a homogeneous isotropic medium [29]. These are calculated for focal mechanism solutions of each seismic event. The P axis bisects the compressional dihedron (45 from both focal planes) [30]. Table-2 shows moment stress axes depending on their azimuth and Figure-7 shows that, in the study area, the major compressional orientation was mostly is NE–SW and W-E, with NW-SE in northern and northeastern parts of the region.

5.3 Moment magnitude (Mw) versus local magnitude Ml

Magnitude is used as an expression for energy releases from an earthquake. Most of the instrumental data around the world use the local magnitude (Ml) scale that covers the entire magnitude

range from potentially less than zero and up to 6 or more. The suitable conversion from local magnitude (Ml) to moment magnitude (M*w*) is a significant prerequisite for any seismic-hazard assessment [31]. Local magnitude is the primary magnitude scale calculated in the department of Seismology in Iraqi Meteorological Organization and Seismology for the 102 events in this study, which ranged from 4.0 to 6.4. Moment magnitude derived from moment tensor techniques, ranged from 3.67 to 6.11 (Table 2).

The developed relation between local magnitude (Ml) and moment magnitude (M*w*) is derived by a linear relation, as shown in Figure- 8 and expressed as follows:

$$Mw = 0.962Ml + 0.0534 \ (R^2 = 0.8877)$$

where: a = 0.962, b = 0.0534 and R^2 represents the correlation coefficient.

In most of the events, the value of M*w* from moment tensor inversions was less than the reported Ml. The average difference was in the order of 0.33 magnitude units. There is a feasible acceptance for events with magnitudes of 4 to 6.5, indicating that the Ml and magnitude body wave (mb) are equal or more than M*w* [32].

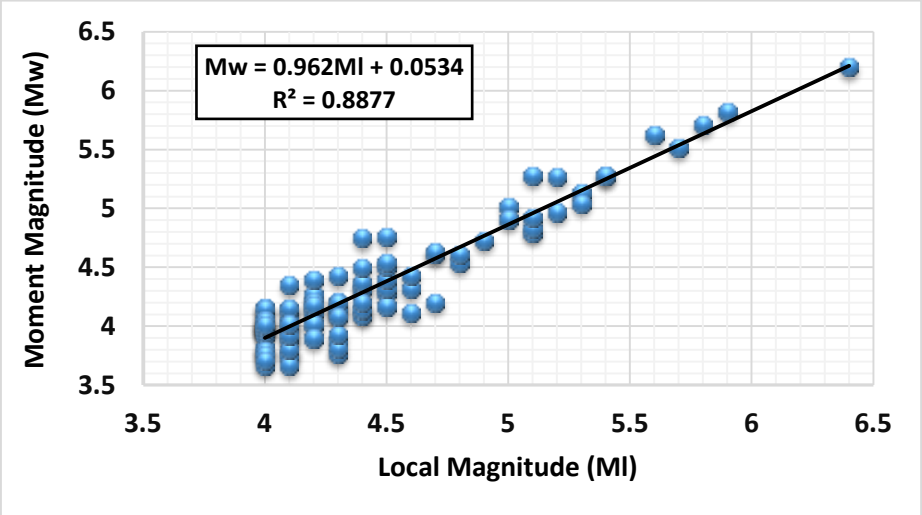

Figure 8- Diagram showing the relationship between local magnitude (Ml) taken from the IMOS catalog and the moment magnitude (Mw) resulted from moment tensor inversion solutions during the current study. The continuous line represents the best least-square fits obtained in this study.

6. Discussion

In this paragraph, we will discuss the results of the moment tensor inversion of all events, their tectonic context, and the active tectonic structures. For each event, moment tensor inversion was used to determine source mechanisms from the regional waveforms. The use of individual focal mechanisms for the assessment of the tectonic stress is not a direct solution, since the degree that they sample intrinsic tectonic episodes varies. This is due to several uncertainties related to inherent ambiguities in the definition of the fault plane and slip direction or to the accuracy of the individual focal mechanisms and the respective inversion methods' assumptions. Previous studies proposed that the earthquakes in the study area likely happen on the Mountain Flexure Fault (sometimes referred to as Main Front Fault, noted MFF in Figure- 2) on blind reverse faults buried under or within a thick, folded sedimentary cover [33]. Along the major part of the Zagros belt, the MFF follows a NW-SE axis with a ~ 120◦ azimuth and corresponds to many topographic lineaments. The next sections will debate the focal mechanism or the fault plane solutions, moment magnitudes, and the focal depths in each sub region.

1. **Belula-Ezgeleh (group AA):** The Northern part of the study region is located on the border of Iraq-Iran within the Zagros fold and thrust belt, which delimits the continental collision between the Arabian and Eurasian Plates. Only six focal mechanisms exist for this sub-region. The resulting fault plane solutions for all the studied earthquakes demonstrate thrust faulting with a strike-slip (5events)

and strike slip pure (one event). Stress tensor suggests that compression is homogeneous in a nearly horizontal NE-SW direction and the combination of thrust with strike-slip faulting.

2. **Khanaqin-Qasre Shirin-Sarpol Zahab (group BB).** This group represents the largest number of events (45 events). Most of them are inside Iran and a few on the Iraq-Iran border, located within the Zagros fold and thrust belt, which is a very seismically active region. A tectonically effective region that accommodates crustal shortening resulting from the collision between the Arabian plate and the Eurasian plate is observed as a differential tectonic movement divided between different types of faults [34]. Local structural complexities may explain why the Qasre Shirin sequence broke in earthquakes series of moderate events rather than as a single thoroughgoing larger rupture with NW striking segments, which is parallel to the regional trend in the fold axes [35]. Thrust faulting with almost all compression axes in the northeastern to southwest orientations characterizes the solutions, including a larger proportion of thrust and thrust with strike slip focal mechanisms, while a few pure strike slip and unknown or oblique slips were present (Table- 2, Figure- 7).

3. **Mandali-Samoor (CC):** Most of the events in this group are distributed on the border between Iraq and Iran, a few kilometers northeast of the Iranian town of Naft Shahr (Figure- 7). 29 focal mechanisms exist for this group, dominantly showing thrust faulting. All events have predominantly thrust mechanisms with reasonably dipping (∼50–80◦), approximately NNW or approximately SSE striking nodal planes (Table-2).

4. **DD (Qolqoleh-Halol):** The Qolqoleh-Halol is located in the western part of the study area. All the 22 seismic events are located inside Iran between High Zagros Fault and Main Recent Fault. This is a major NW-SE, 800-km-long right lateral strike-slip fault that accommodates some of the strain [36] (Figure- 2).These events form a right lateral strike-slip focal mechanism but are located more than 100 km west of the Main Recent Fault. This group is completely different from the previous groups with its distinction, as 21 focal mechanisms are dominantly strike-slip, with only one event that has a normal faulting. All of these mechanisms reveal a general trend of NW-SE orientation.

7. Conclusions

The present application of the CPS software package allowed us to compute seismic moment tensors for 102 earthquakes by using broadband waveform inversion with an Ml between 4.0 and 6.4. The most distinguishing characteristic in the focal mechanism distributions in the study area is their depth dependence, thus, all of the earthquakes according to the results have crustal depths ranging from 8 to 21 km. The major stress compressional (P) axes orientations are determined from moment tensor solutions of the locally recorded earthquakes that occurred in the study area. Deformation style of the groups (AA, BB, and CC) suggests predominant thrust faulting, thrust with strike-slip faulting component, and some unknown or oblique faulting that indicates compressional or transpressional tectonic environment. However, strike-slip earthquakes (SS) predominate to the west (group DD). Nevertheless, earthquakes are distributed in the study area of faulting in the Zagros range, which is amongst the most rapidly deforming and seismically active fold-and-thrust belts on earth. The majority of seismicity are occurring on the blind reverse faults buried under or within a thick, folded sedimentary cover. Therefore, the distribution of earthquakes provides vital information about the location of active faulting at depth.

Good matching results were obtained in the current study with both seismic trends (concluded from earthquake locations) and mapped faults. These matching results are corresponding with the tectonic framework of the Arabian–Eurasian continental collision zone and the anticlockwise rotation of the Arabian plate that appears accountable for strike-slip displacements on fault surfaces. Also, a relation between moment and local magnitude was obtained appropriately for the investigated area and magnitude range.

Acknowledgement

The authors would like to extend their appreciation to Dr. Wathiq Abdulnaby of Seismological Laboratory of University of Basrah (SLUB) for his great assistance scientific and for providing the data in this research. Also, we wish to express our gratitude to the Mr. Fadhil Ibrahim director-general of the Directorate of Meteorology and Seismology, Erbil, Iraq to provide some of the data seismic. Our thanks and appreciation to Dr. Mohammadreza Jamal-Reyhan at the Institute of Geophysics,

University of Tehran (IGUT) for his scientific contribution. Our thanks to Tiesheng Wu, Hainan Research Center of Engineering Earthquake- China Earthquake Administration for using his tool's ArcBeachBalls_v2.3.

References

1. Talukdar, P. and Barman, N. C. **2012**. Seismic activity and seismotectonic correlation with reference to northeast India. *IOSR Journal of Applied Physics*, **2**(2): 24-29. https://doi.org/10.9790/4861-0222429.
2. Ghalib, H. A. and Alsinawi, S.A. **1974**. On The Seismotectonics of the Arabian Peninsula-*A Global Tectonic Approach. Bull. Coll. Sci.***15**:151-169.
3. Alridha, N.A. and Mohammed, H.J. 2015. Seismicity Study of Khanaqin Area, Iraqi Journal of Science, **56**(1A): 181 – 190. https://www.iasj.net/iasj?func=fulltext&aId=99402.
4. Alridha, N. A., Baqir, R. A. and Hamid, A. R. **2012**. Seismicity and seismotectonic study for Altunkopri dam site north Iraq. *Iraqi Journal of Science*, **53**(3): 595-601. https://www.iasj.net/iasj?func=article&aId=62807.
5. Scharf, A., Mattern, F. and Al-Sadi, S. S. **2016**. Kinematics of Post-obduction Deformation of the Tertiary Ridge at Al-Khod Village (Muscat, Oman). *Sultan Qaboos University Journal for Science [SQUJS]*, **21**(1): 26-40. DOI: http://dx.doi.org/10.24200/squjs.vol21iss1pp26-40.
6. Sissakian, V.K. **2000**. *Geological Map of Iraq*, 3 rd edit., scale 1: 1000000. GEOSURV, Baghdad, Iraq.
7. Fouad, S.F. **2015**. Tectonic map of Iraq, *scale 1:1000000*, 3rd ed. Iraqi Bull. Geol. Min. **11** (1),1-7. https://www.iasj.net/iasj?func=fulltext&aId=99665.
8. Zebari, M., Grützner, C., Navabpour, P. and Ustaszewski, K. **2019**. Relative timing of uplift along the Zagros Mountain Front Flexure (Kurdistan Region of Iraq): Constrained by geomorphic indices and landscape evolution modeling. *Solid Earth*, **10**(3): 663-682. https://doi.org/10.5194/se-10-663-2019.
9. Herrmann, R. B. and Ammon, C. J. **2004.** Source inversion, In: *Computer programs in seismology, version 3.30*, Saint Louis University, Missouri.
10. Sissakian, V., Al-Ansari, N., and Knutsson, S., **2014**. Origin of some transversal linear features of NE-SW trend in Iraq, and their geological characters. *Natural Science*, **6**(12): 996-1011. http://dx.doi.org/10.4236/ns.2014.612091.
11. Jackson, J., R. Norris and Youngson, **J. 1996**. The structural evolution of active fault and fold systems in central Otago, New Zealand: Evidence revealed by drainage patterns. *Journal of Structural Geology*,**18**: 217-234. https://doi.org/10.1016/S0191-8141(96)80046-0.
12. Dercourt, J., Zonenshain, L. P., Ricou, L. E., Kazmin, V. G., Le Pichon, X., Knipper, A. L. and Pechersky,D. H. **1986**. Geological evolution of the Tethys belt from the Atlantic to the Pamirs since the Lias. Tectonophysics, **123**(1-4):241-315.https://doi.org/10.1016/0040-1951(86)90199-X.
13. Fouad, S.F. **2014**. Western Zagros Fold – Thrust Bekt, Part II. In: The geology of the High Folded Zone. *Iraqi Bull Geol. Min., Special Issue*, **6**: 57-75. http://ibgm-iq.org/ibgm/index.php/ibgm/article/view/275.
14. Jassim, S. Z. and Goff, J. C. **2006**. *Geology of Iraq*. DOLIN, distributed by Geological Society of London.
15. Karasözen, E., Nissen, E., Bergman, E. A. and Ghods, A. **2019**. Seismotectonics of the Zagros (Iran) From Orogen-Wide Calibrated Earthquake Relocations. *Journal of Geophysical Research: Solid Earth*, **124**(8): 9109-9129. https://doi.org/10.1029/2019JB017336.
16. Berberian, M. **1995**. Master "blind" thrust faults hidden under the Zagros folds: active basement tectonics and surface morphotectonics. *Tectonophysics*, **241**(3-4): 193-224. https://doi.org/10.1016/0040-1951(94)00185-C.
17. Alavi, M. **2004**. Regional stratigraphy of the Zagros Fold-thrust belt of Iran and its pro-foreland evolution. *American Journal of Science*, **304**: 1-20. https://ui.adsabs.harvard.edu/link_gateway/2004AmJS..304....1A/doi:10.2475/ajs.304.1.1.
18. Vergés, J., Goodarzi, M. G. H., Emami, H., Karpuz, R., Efstathiou, J. and Gillespie, P. **2011**. Multiple detachment folding in Pusht-e Kuh arc, Zagros: Role of mechanical stratigraphy.
19. Ramsey, L.A., Walker, R.T. and Jackson, J. **2008**. Fold evolution and drainage development in the Zagros Mountains of Fars province, SE Iran. *Basin Research*, **20**(1): 23-48.

https://doi.org/10.1111/j.1365-2117.2007.00342.x.

20. Berberian, M. **1981**. *Active faulting and tectonics of Iran, Zagros Hindu Kush Himalaya Geodynamic Evolution*. Washington, DC: American Geophysical Union. https://doi.org/10.1029/GD003p0033.

21. Hollingsworth, J., Fattahi, M., Walker, R., Talebian, M., Bahroudi, A., Bolourchi, M. J. and Copley, A. **2010**. Oroclinal bending, distributed thrust and strike-slip faulting, and the accommodation of Arabia–Eurasia convergence in NE Iran since the Oligocene. *Geophysical Journal International*, **181**(3): 1214-1246. https://doi.org/10.1111/j.1365-246X.2010.04591.x.

22. Nilforoushan, F., Masson, F., Vernant, P., Vigny, C., Martinod, J., Abbassi, M. and Ashtiani, A. **2003**. GPS network monitors the Arabia-Eurasia collision deformation in Iran. Journal of Geodesy, **77**(7-8): 411-422. https://doi.org/10.1007/s00190-003-0326-5.

23. McQuarrie, N., Stock, J.M., Verdel, C. and Wernicke, B.P. **2003**. Cenozoic evolution of Neotethys and implications for the causes of plate motions. *Geophys. Res. Lett*. **30**(20). https://doi.org/10.1029/2003GL017992.

24. Cesca, S. and Heimann, S. **2013**. A practical on moment tensor inversion using the Kiwi tools. New Manual of Seismological Observatory Practice (NMSOP), **2**: 1-24. https://doi.org/10.2312/GFZ.NMSOP-2_EX_3.6.

25. Stroujkova, A., Reiter, D. T. and Shumway, R. H. **2007**. Regional Seismic Focal Depth Estimation in Complex Tectonic Environments. Weston Geophysical Corp Westborough ma.

26. Dahmn, T. **1996**. Relative moment tensor inversion based on ray theory: theory and synthetic tests. *Geophysical Journal International*, **124**: 245-257. https://doi.org/10.1111/j.1365-246X.1996.tb06368.x.

27. Abdulnaby, W. G. **2013**. Seismotectonics of the northeastern margin of the Arabian plate in Iraq (Doctoral dissertation, University of Arkansas at Little Rock).

28. Alridha, N. A. and Jasem, N. A. **2013**. Seismicity evaluation of central and southern Iraq. *Iraqi Journal of Science*, **54**(4): 911-918. https://www.iasj.net/iasj?func=article&aId=79466.

29. Vavryčuk, V. **2014**. Iterative joint inversion for stress and fault orientations from focal mechanisms. *Geophys J Int*, **199**(1): 69–77. https://doi.org/10.1093/gji/ggu224.

30. Anderson, E.M. **1951**. *The Dynamics of Faulting and Dyke Formation with Applications to Britain.* Oliver and Boyd, Edinburgh, 206p.

31. Deichmann, N. **2017**. Theoretical basis for the observed break in ML/MW scaling between small and large earthquakes. *Bull. Seismol. Soc. Am*, **107**(2): 505–520. https://doi.org/10.1785/0120160318.

32. Kanamori, H. **1983**. Magnitude scale and quantification of earthquakes. Tectonophysics, **93** (3-4): 185-199. https://doi.org/10.1016/0040-1951(83)90273-1.

33. Barnhart, W. D., Brengman, C. M., Li, S. and Peterson, K. E. **2018**. Ramp-flat basement structures of the Zagros Mountains inferred from co-seismic slip and after slip of the 2017 Mw7. 3 Darbandikhan, Iran/Iraq earthquake. *Earth and Planetary Science Letters*, **496**: 96-107.

34. Berberian, M. and King, G. C. P. **1981**. Towards a paleogeography and tectonic evolution of Iran. *Canadian Journal of Earth Sciences*, **18**(2): 210–265. https://doi.org/10.1016/j.epsl.2018.05.036.

35. Nissen, E., Ghods, A., Karasözen, E., Elliott, J. R., Barnhart, W. D., Bergman, E. A. and Abdulnaby, W. **2019**. The 12 November 2017 M w 7.3 Ezgeleh-Sarpolzahab (Iran) Earthquake and Active Tectonics of the Lurestan Arc. *Journal of Geophysical Research: Solid Earth*, **124**(2): 2124-2152. https://doi.org/10.1029/2018JB016221.

36. Tchalenko, J. S. and Braud, J. **1974**. Seismicity and structure of the Zagros (Iran): the Main Recent Fault between 33 and 35 N. Philosophical Transactions of the Royal Society of London. Series A, *Mathematical and Physical Sciences*, **277**(1262): 1-25. https://doi.org/10.1098/rsta.1974.0044.